

**TTL cirrus and water
transport**

T. Dinh et al.

Cirrus and water vapor transport in the tropical tropopause layer: a modeling study

T. Dinh, D. R. Durrán, and T. Ackerman

Department of Atmospheric Sciences, University of Washington, Seattle, Washington 98195, USA

Received: 31 March 2012 – Accepted: 2 April 2012 – Published: 25 April 2012

Correspondence to: T. Dinh (tradinh@uw.edu)

Published by Copernicus Publications on behalf of the European Geosciences Union.

Title Page

Abstract

Introduction

Conclusions

References

Tables

Figures

◀

▶

◀

▶

Back

Close

Full Screen / Esc

Printer-friendly Version

Interactive Discussion



Abstract

We carry out simulations of tropical-tropopause-layer (TTL) cirrus which are formed and forced by a large-scale equatorial Kelvin wave. We find that, even under the influence of the large-scale wave, the radiatively induced mesoscale dynamics in TTL cirrus actively contributes to transport of water vapor in the vertical direction.

In a typical TTL cirrus, the heating that results from absorption of radiation by ice crystals induces a mesoscale circulation. Advection of water vapor by the radiatively induced circulation leads to upward advection of the cloudy air. Upward advection of the cloudy air is equivalent to upward transport of water vapor when the air above the cloud is drier than the cloudy air. On the other hand, ice nucleation and depositional growth, followed by sedimentation and sublimation lead to downward transport of water vapor. The net direction of transport is determined by the relative magnitudes of the upward advection of water vapor and the downward transport associated with microphysical processes.

1 Introduction

Stratospheric water vapor plays an important role in the chemistry of the stratosphere and in the radiation budget of the atmosphere. It originates from either the oxidation of methane in the stratosphere, or the transport of water vapor from the troposphere to the stratosphere. The latter occurs mainly in the transition layer between the troposphere and the stratosphere in the tropics, referred to as the *tropical tropopause layer* (TTL).

It was proposed that the mass of water vapor transported into the stratosphere is limited by the freeze-drying of the air in the TTL in the ascending branch of the Brewer-Dobson circulation (Brewer, 1949). According to this, the tropopause acts as a cold trap at which water vapor in the rising air condenses into ice, which is then removed by sedimentation. The abundance of thin cirrus in the TTL, hereafter referred to as TTL cirrus, provides the evidence that freezing indeed occurs frequently there.

TTL cirrus and water transport

T. Dinh et al.

Title Page

Abstract

Introduction

Conclusions

References

Tables

Figures

◀

▶

◀

▶

Back

Close

Full Screen / Esc

Printer-friendly Version

Interactive Discussion



TTL cirrus and water transport

T. Dinh et al.

[Title Page](#)[Abstract](#)[Introduction](#)[Conclusions](#)[References](#)[Tables](#)[Figures](#)[◀](#)[▶](#)[◀](#)[▶](#)[Back](#)[Close](#)[Full Screen / Esc](#)[Printer-friendly Version](#)[Interactive Discussion](#)

TTL cirrus may occur as frequently as 20 to 50 % of the time (Wang et al., 1996; Mace et al., 2009; Virts and Wallace, 2010)) and may persist for days (Winker and Trepte, 1998; Taylor et al., 2011). Most of these clouds occur just below the tropopause (Wang et al., 1996; Peter et al., 2003). They are typically less than one kilometer thick, but hundreds of kilometers wide (Winker and Trepte, 1998; Thomas et al., 2002; Peter et al., 2003; Lawson et al., 2008). A few TTL cirrus have been observed to be as wide as 2000 to 3000 km (Winker and Trepte, 1998; Lawson et al., 2008; Taylor et al., 2011). Half of TTL cirrus may have formed in situ; the other half are remnants of convective anvils (Massie et al., 2002). Only TTL cirrus that are formed in situ will be studied here.

Although TTL cirrus are ubiquitous, they do not appear as a continuous cloud sheet covering the entire tropics (Winker and Trepte, 1998). Thus the occurrence of these clouds cannot be attributed solely to the freezing of air slowly rising across the tropopause in the Brewer-Dobson circulation. The low tropopause temperature means that the mean state TTL is pre-conditioned for freezing, but cirrus formation is more likely to occur over regions that are moister and/or colder than the background.

Holton and Gettelman (2001) proposed that freezing occurs preferentially over the equatorial West Pacific during the Northern Hemisphere winter, where the coldest tropopause temperature occurs. They suggested that horizontal transport over this region leads to freeze-drying of the air to a very low water vapor mixing ratio. This hypothesis helps to explain why the stratosphere is drier than the saturation water vapor mixing ratio indicated by the mean tropopause temperature.

In addition to large-scale transport over colder regions of the TTL, cirrus may also form in regions subject to negative temperature anomalies associated with waves in the TTL. Several observational studies show correlations between TTL cirrus occurrence and the cold phases of large-scale equatorial Kelvin waves (Boehm and Verlinde, 2000; Immler et al., 2008; Fujiwara et al., 2009). One may expect that smaller scale gravity waves could also result in TTL cirrus formation on smaller temporal and spatial scales.

An aspect of the freeze-drying hypothesis that remains to be tested is whether freezing is always accompanied by drying. In other words, are TTL cirrus always associated

with stratospheric dehydration? Many studies that associate these clouds with stratospheric dehydration have either neglected TTL cirrus radiative effect (Jensen et al., 1996, 2001; Jensen and Pfister, 2004), or assumed radiative cooling (Hartmann et al., 2001; Holton and Gettelman, 2001). Radiative cooling may occur if TTL cirrus lie above sufficiently cold convective anvils. However, observations and radiative transfer calculations suggest that the radiative effect of TTL cirrus is most likely heating rather than cooling (Comstock et al., 2002; Haladay and Stephens, 2009; Yang et al., 2010). The radiative heating rate in TTL cirrus could be up to a few Kelvins per day (McFarquhar et al., 2000; Comstock et al., 2002; Bucholtz et al., 2010), which is an order of magnitude larger than in clear sky conditions. Using a large-scale model which takes into account TTL cirrus radiative heating, Rosenfield et al. (1998) found that the increase in stratospheric water vapor induced by the radiative heating outweighs the decrease due to ice sedimentation.

In order to fully account for the radiative effect in TTL cirrus, the dynamics induced by the radiative heating must be considered. Studies by Durran et al. (2009) and Dinh et al. (2010) suggested that the radiative heating in TTL cirrus forces a mesoscale circulation with rising motion in the vertical column containing the cloud, subsidence to the east and west of the cloud, and horizontal inflow and outflow respectively in the lower and upper half of the cloud layer. This radiatively induced dynamics may maintain TTL cirrus over several days in an otherwise quiet atmosphere (Dinh et al., 2010). However, Jensen et al. (2011) found in their numerical simulations that, when subject to external wind shear, TTL cirrus dissipate before the radiatively induced dynamics could develop.

The goal of this work is to investigate the role of TTL cirrus in the dehydration of the TTL considering the radiative, dynamical and microphysical processes in these clouds. The influence from a large-scale equatorial Kelvin wave is also taken into account. We test whether the radiatively induced dynamics in TTL cirrus persist and impact the water vapor transport under a realistic spatially and temporally varying shear of the large-scale wave.

TTL cirrus and water transport

T. Dinh et al.

[Title Page](#)[Abstract](#)[Introduction](#)[Conclusions](#)[References](#)[Tables](#)[Figures](#)[◀](#)[▶](#)[◀](#)[▶](#)[Back](#)[Close](#)[Full Screen / Esc](#)[Printer-friendly Version](#)[Interactive Discussion](#)

The article is organized as follows. The basis of the model used in this research is described in Sect. 2. The method to apply the large-scale wave forcing on clouds is explained in Sect. 3. Simulations of TTL cirrus life cycle and transport of water vapor are described in Sect. 4. Section 6 contains the conclusions.

2 Model basis

All simulations are currently restricted to two dimensions. Let x and z denote the location along the horizontal and vertical axes. Let t denote time.

We write pressure p as the sum of a static base state \tilde{p} and a dynamic perturbation component p' :

$$p(x, z, t) = \tilde{p}(z) + p'(x, z, t), \quad (1)$$

where the tilde over the variable denotes the base state and the prime by the variable denotes the dynamic perturbation. $\tilde{p}(z)$ is a function of z only, while $p'(x, z, t)$ varies with x , z and t . Similar relations are defined for other thermodynamic state variables: temperature T , potential temperature θ , virtual potential temperature $\theta_v = \theta(1 + 0.61q_v - q_i)$, and air density ρ . Similar relations also hold for water vapor mixing ratio q_v and ice mixing ratio q_i . However, the base state ice mixing ratio is zero $\tilde{q}_i = 0$. Other microphysical species such as liquid water and snow are not relevant to TTL cirrus.

Based on the anelastic approximation, the conservation laws of air mass, momentum, potential temperature, water vapor and ice mixing ratios in a frictionless, two-dimensional atmosphere are (Bannon, 2002, Appendix B)

$$\nabla \cdot (\tilde{\rho} \mathbf{u}) = 0, \quad (2)$$

$$\frac{\partial \mathbf{u}}{\partial t} + (\mathbf{u} \cdot \nabla) \mathbf{u} = -\nabla \left(\frac{p'}{\tilde{\rho}} \right) + g \frac{\theta'_v}{\tilde{\theta}_v} \mathbf{k}, \quad (3)$$

TTL cirrus and water transport

T. Dinh et al.

Title Page

Abstract

Introduction

Conclusions

References

Tables

Figures

◀

▶

◀

▶

Back

Close

Full Screen / Esc

Printer-friendly Version

Interactive Discussion



$$\frac{\partial \theta'}{\partial t} + \mathbf{u} \cdot \nabla (\bar{\theta} + \theta') = \frac{\dot{Q}\theta}{c_v T}, \quad (4)$$

$$\frac{\partial q'_v}{\partial t} + \mathbf{u} \cdot \nabla (\bar{q}_v + q'_v) = -S, \quad (5)$$

$$\frac{\partial q'_i}{\partial t} + \mathbf{u} \cdot \nabla q'_i - V_t \frac{\partial q'_i}{\partial z} = S + \mathcal{J}, \quad (6)$$

where c_v is the specific heat of air at constant volume, g is the gravitational acceleration constant on Earth, \mathbf{k} is the unit vector in the vertical direction, $\mathbf{u} = (u, w)$ is the velocity vector, V_t is the terminal fall speed of ice crystals, S is the ice mass depositional growth rate per unit air mass, \mathcal{J} is the ice mass nucleation rate per unit air mass, and \dot{Q} is the diabatic heating rate per unit air mass. The diabatic heating includes radiative and latent heat. In TTL cirrus the latent heat release is negligible compared to the radiative heating.

Substituting the divergence of Eq. (3) into the time derivative of Eq. (2) we obtain an elliptic partial differential equation for pressure

$$\nabla \cdot \left(\bar{\rho} \nabla \left(\frac{p'}{\bar{\rho}} \right) \right) + \nabla \cdot (\bar{\rho} (\mathbf{u} \cdot \nabla) \mathbf{u}) = \frac{\partial}{\partial z} \left(\bar{\rho} g \frac{\theta'_v}{\bar{\theta}_v} \right). \quad (7)$$

Eqs. (3)–(7) form a set of governing equations used to solve for \mathbf{u} , θ' , q'_v , q'_i and p' in the model. The dynamical core of the System of Atmospheric Modeling developed by Khairoutdinov and Randall (2003) is used here to solve Eqs. (3) and (7) for \mathbf{u} and p' . The selective-monotonicity-preserving advection scheme developed by Blossey and Durran (2008) is used to compute the terms involving $\mathbf{u} \cdot \nabla$ in Eqs. (4)–(6). The diabatic heating rate \dot{Q} in Eq. (4), which comprises mostly of the absorption of longwave radiation by ice crystals, is computed by the radiation scheme described in Durran et al.

TTL cirrus and water transport

T. Dinh et al.

Title Page

Abstract

Introduction

Conclusions

References

Tables

Figures

◀

▶

◀

▶

Back

Close

Full Screen / Esc

Printer-friendly Version

Interactive Discussion



(2009). The source term S in Eqs. (5) and (6) is computed by the bin microphysics scheme originally designed by Chen and Lamb (1994), later modified by Dinh and Duran (2012). Ice crystals are assumed spherical and distributed into 25 bins ranging from $0.25\ \mu\text{m}$ to $25\ \mu\text{m}$ in radius. V_t in Eq. (6) is computed following the formula of terminal fall velocity deduced by Böhm (1989). Ice nucleation \mathcal{J} is based on the formula for homogeneous freezing derived experimentally by Koop et al. (2000). We assume a background aerosol with concentration $100\ \text{cm}^{-3}$ and radius $0.25\ \mu\text{m}$. The deposition coefficient of water vapor on ice is assumed to be 0.01, which is larger than the experimental value suggested by Magee et al. (2006) but smaller than those suggested by cloud modelers (e.g. Kay and Wood (2008)). Sensitivity of our model results to the deposition coefficient will be discussed in a subsequent paper. Other details of the bin microphysics scheme can be found in Dinh et al. (2010).

3 Equatorial Kelvin waves

TTL cirrus occurrences that are closely correlated with the cold phases of large-scale equatorial Kelvin waves have been observed (Boehm and Verlinde, 2000; Immler et al., 2008; Fujiwara et al., 2009). During the cold phases of the waves, negative temperature anomalies increase the relative humidity. If the air is sufficiently moist, ice crystals are nucleated and then grow by deposition of water vapor. In addition to the temperature perturbations, the large-scale waves exert spatially and temporally varying shears on the clouds. With the temperature perturbations and shear associated with a large-scale equatorial Kelvin wave added as external disturbances on the cloud, we can compare our model results with those by Jensen et al. (2001). In their simulations, steady wind shear leads to dissipation of TTL cirrus before the radiative heating can drive a circulation to maintain the clouds. The wind shear in their simulations is prescribed to be uniform and steady, whereas our shear varies in space and time consistently with the propagation the equatorial Kelvin wave.

Title Page

Abstract

Introduction

Conclusions

References

Tables

Figures

◀

▶

◀

▶

Back

Close

Full Screen / Esc

Printer-friendly Version

Interactive Discussion



TTL cirrus and water transport

T. Dinh et al.

Title Page

Abstract

Introduction

Conclusions

References

Tables

Figures

◀

▶

◀

▶

Back

Close

Full Screen / Esc

Printer-friendly Version

Interactive Discussion



Observational data of equatorial Kelvin waves are available but are difficult to be used in simulations. Observational fields are not necessarily dynamically consistent with one another and may not be at the desired temporal and spatial resolution and coverage. Hence we generate the wave numerically.

This section describes the procedure to first generate the numerical solution for an equatorial Kelvin wave (Sect. 3.1) and then apply the wave as external forcing on TTL cirrus (Sect. 3.2). Modeling the large-scale wave and cirrus clouds require different temporal and spatial resolution as well as simulation duration and domain size. To ensure efficiency the large-scale wave is first generated in a cloud-free, coarse resolution simulation (the *large-scale wave simulation*). Then, the wave solution is interpolated to finer resolution and used to drive the *TTL cirrus simulation*. The large-scale wave simulation is described in Sect. 3.1, and the TTL cirrus simulation is described in Sect. 4.

3.1 Generating the large-scale wave

3.1.1 Method

An equatorial Kelvin wave is excited in the model by forcing the vertical velocity within a forcing region towards an oscillating solution. For every time step, all x , and $z_f - H \leq z \leq z_f + H$, we set

$$w_f = w_0 \cos(kx - lz - \omega t), \quad (8)$$

$$\alpha = \cos^2 \left(\frac{\pi(z - z_f)}{2H} \right), \quad (9)$$

$$w^{\text{new}} = (1 - \alpha)w^{\text{old}} + \alpha w_f, \quad (10)$$

where w_0 is the magnitude of the prescribed vertical velocity w_f , w^{old} is the vertical velocity given by the model at the current time step, w^{new} is the vertical velocity after it is forced towards w_f , z_f is the altitude at the center of the forcing region, H is half

the depth of the forcing region, k and l are respectively the horizontal and vertical wavenumbers and ω is the frequency. The factor α as defined by Eq. (9) specifies the degree by which the vertical velocity is forced towards w_f ; α decreases smoothly from one at the center of the forcing region to zero at the top and base of the forcing region.

When the vertical velocity is forced according to Eqs. (8)–(10), wave energy from the forcing region radiates upwards generating an internal gravity wave above the forcing region. As defined by Eq. (8), the phase velocity of the wave is eastward and downward and the group velocity is eastward and upwards. In our two-dimensional domain (the vertical plane along the equator), equatorial Kelvin waves have the same structure as these internal gravity waves.

The free parameters to be specified as input to the large-scale wave simulation are w_0 , H , z_f , and any two of the three parameters k , l and ω . The parameters k , l and ω are related by the dispersion relation for internal gravity waves, which is

$$\omega^2 = \frac{k^2 N^2}{k^2 + l^2},$$

where N is the Brunt-Väisälä frequency.

3.1.2 Configuration of the large-scale wave simulation

The sounding used here and throughout simulations in Sect. 4 is from balloon-borne measurements on 7 January 2007 over Nauru island (0.521° S, 166.916° E). The temperature profile on this date has a distinctive minimum at the tropopause typical of tropical soundings. The sounding data were obtained from the Atmospheric Radiation Measurement (ARM) Program. A few modifications are applied to the raw temperature data. Above 12.0 km, a smoothing algorithm is applied to remove small scale fluctuations. Below 12.0 km, observed temperature data are replaced by values computed by assuming that the Brunt-Väisälä frequency is constant and equal to the Brunt-Väisälä frequency at 12.0 km. In the layer in the vicinity of the tropopause between 16.0 km and 17.5 km, the temperature is modified such that the Brunt-Väisälä frequency is at least

TTL cirrus and water transport

T. Dinh et al.

Title Page

Abstract

Introduction

Conclusions

References

Tables

Figures

◀

▶

◀

▶

Back

Close

Full Screen / Esc

Printer-friendly Version

Interactive Discussion



TTL cirrus and water transport

T. Dinh et al.

Title Page

Abstract

Introduction

Conclusions

References

Tables

Figures

◀

▶

◀

▶

Back

Close

Full Screen / Esc

Printer-friendly Version

Interactive Discussion



0.0125 s^{-1} . These modifications to the raw data ensure that the atmospheric profile is sufficiently stable. If the atmosphere is initially unstable or becomes unstable due to perturbations developed during the simulation, the response to the forcing in the vertical velocity (Eqs. 8–10) is dominated by convection, rather than large-scale waves. The temperature and potential temperature of the raw and modified soundings are shown in Fig. 1. The Brunt-Väisälä frequency of the modified sounding is also shown in Fig. 1. The Brunt-Väisälä frequency computed from the raw sounding contains small-scale large-amplitude noise that cannot be conveniently plotted on the same scale.

For this simulation, we set $w_0 = 1.8 \text{ mm s}^{-1}$, $H = 4 \text{ km}$, $z_f = 6 \text{ km}$, $k = 1.047 \times 10^{-5} \text{ m}^{-1}$ and $\omega = 1.212 \times 10^{-5} \text{ s}^{-1}$ in Eqs. (8)–(10). These values of k and ω correspond to a horizontal wavelength of 6000 km and a wave period of 6 day. The horizontal domain is equal to the horizontal wavelength. Periodic boundary conditions are applied at the lateral boundaries. The bottom of the domain is at $z = 0$ and the top of the domain is at $z = 20 \text{ km}$. A non-reflective open boundary condition (Bougeault, 1983; Klemp and Durran, 1983) is applied at the top and bottom of the domain. The resolution is $\Delta x = 20 \text{ km}$ in the horizontal and $\Delta z = 100 \text{ m}$ in the vertical. The time step is $\Delta t = 30 \text{ s}$. The simulation is from $t = 0$ to $t = 120 \text{ day}$. The simulation time must be sufficiently long to allow the forced wave to reach steady state oscillations.

3.1.3 Wave solution

The numerical solution reaches steady oscillations after about 60 day (ten wave cycles). Thus the solution at any time after 60 day can be taken as large-scale equatorial Kelvin waves. In the 12-day-simulations of clouds presented in Chapter 4, we choose to use the wave solution between 92 day and 104 day and in the region $z \geq 15 \text{ km}$. Since 15 km is well above the region in which w is forced towards w_f , the solution in the forcing region is avoided.

The wave temperature perturbations through the center of the domain ($x = 3000 \text{ km}$) as a function of altitude and time between 92 day and 104 day are shown in Fig. 2. The

wave vertical and horizontal velocities and temperature perturbations at $t = 92$ day are shown as functions of x and z in Fig. 3. The positive and negative peaks of the wave are not mirrors of one another because the wave amplitude is sufficiently large that nonlinearity becomes important.

The amplitude of the temperature perturbations is larger above than below the cold point tropopause (CPT) at $z = 17.3$ km (Figs. 2 and 3) because of the sharp increase with altitude of the Brunt-Väisälä frequency there (see Fig. 1). Observed equatorial Kelvin waves also exhibit this behavior at the tropopause (see Immler et al. (2008, Fig. 1) and Boehm and Verlinde (2000, Fig. 1)).

The amplitude of the temperature perturbations near the tropopause is 2.0 to 2.5 K in this simulation. Temperature perturbations in Kelvin waves were observed by Immler et al. (2008) to be up to 8 K, but typically 2 to 3 K.

3.2 Imposing large-scale wave forcing on clouds

Here we derive a set of governing equations applicable to the TTL cirrus simulation under the influence of the large-scale equatorial Kelvin wave. The large-scale wave solution is available beforehand and assumed to be unaffected by the clouds. Let the subscript “ls” denote large-scale waves, and “c” denote clouds.

In the large-scale wave simulation, Eqs. (3)–(5) and (7) correspond to

$$\frac{\partial \mathbf{u}_{ls}}{\partial t} + (\mathbf{u}_{ls} \cdot \nabla) \mathbf{u}_{ls} = -\nabla \left(\frac{\rho'_{ls}}{\tilde{\rho}} \right) + g \frac{\theta'_{v,ls}}{\tilde{\theta}_v} \mathbf{k}, \quad (11)$$

$$\frac{\partial \theta'_{ls}}{\partial t} + \mathbf{u}_{ls} \cdot \nabla (\tilde{\theta} + \theta'_{ls}) = 0, \quad (12)$$

$$\frac{\partial q'_{v,ls}}{\partial t} + \mathbf{u}_{ls} \cdot \nabla (\tilde{q}_v + q'_{v,ls}) = 0, \quad (13)$$

Title Page

Abstract

Introduction

Conclusions

References

Tables

Figures

◀

▶

◀

▶

Back

Close

Full Screen / Esc

Printer-friendly Version

Interactive Discussion



$$\nabla \cdot \left(\tilde{\rho} \nabla \left(\frac{\rho'_{\text{ls}}}{\tilde{\rho}} \right) \right) + \nabla \cdot (\tilde{\rho} (\mathbf{u}_{\text{ls}} \cdot \nabla) \mathbf{u}_{\text{ls}}) = \frac{\partial}{\partial z} \left(\tilde{\rho} g \frac{\theta'_{\text{v,ls}}}{\tilde{\theta}_{\text{v}}} \right). \quad (14)$$

The right hand sides of Eqs. (12) and (13) are zero because q_i is assumed to be zero in the large-scale wave simulation.

In the TTL cirrus simulation, the velocity vector and the dynamic pressure perturbation are written as the sum of a component associated with the large-scale wave and another induced by the clouds:

$$\begin{aligned} \mathbf{u} &= \mathbf{u}_{\text{c}} + \mathbf{u}_{\text{ls}}, \\ \rho &= \tilde{\rho} + \rho'_{\text{c}} + \rho'_{\text{ls}}, \end{aligned}$$

where for consistency the base state must be the same as that in the large-scale wave simulation. Similar relations hold for other thermodynamic state variables and water vapor mixing ratio. For ice mixing ratio, this reduces to $q_i = q'_{i,\text{c}}$ because $\tilde{q}_i = 0$ and $q'_{i,\text{ls}} = 0$. Hence, Eqs. (3)–(7) correspond to

$$\frac{\partial}{\partial t} (\mathbf{u}_{\text{c}} + \mathbf{u}_{\text{ls}}) + ((\mathbf{u}_{\text{c}} + \mathbf{u}_{\text{ls}}) \cdot \nabla) (\mathbf{u}_{\text{c}} + \mathbf{u}_{\text{ls}}) = \nabla \left(\frac{\rho'_{\text{c}} + \rho'_{\text{ls}}}{\tilde{\rho}} \right) + g \frac{\theta'_{\text{v,c}} + \theta'_{\text{v,ls}}}{\tilde{\theta}_{\text{v}}} \mathbf{k}, \quad (15)$$

$$\frac{\partial}{\partial t} (\theta'_{\text{c}} + \theta'_{\text{ls}}) + (\mathbf{u}_{\text{c}} + \mathbf{u}_{\text{ls}}) \cdot \nabla (\tilde{\theta} + \theta'_{\text{c}} + \theta'_{\text{ls}}) = \frac{\dot{Q}\theta}{c_{\text{v}} T}, \quad (16)$$

$$\frac{\partial}{\partial t} (q'_{\text{v,c}} + q'_{\text{v,ls}}) + (\mathbf{u}_{\text{c}} + \mathbf{u}_{\text{ls}}) \cdot \nabla (\tilde{q}_{\text{v}} + q'_{\text{v,c}} + q'_{\text{v,ls}}) = -S, \quad (17)$$

$$\frac{\partial q'_{i,\text{c}}}{\partial t} + (\mathbf{u}_{\text{c}} + \mathbf{u}_{\text{ls}}) \cdot \nabla q'_{i,\text{c}} - V_{\text{t}} \frac{\partial q'_{i,\text{c}}}{\partial z} = S + J, \quad (18)$$

TTL cirrus and water transport

T. Dinh et al.

Title Page

Abstract

Introduction

Conclusions

References

Tables

Figures

◀

▶

◀

▶

Back

Close

Full Screen / Esc

Printer-friendly Version

Interactive Discussion



$$\nabla \cdot \left(\tilde{\rho} \nabla \left(\frac{\rho'_c + \rho'_{ls}}{\tilde{\rho}} \right) \right) + \nabla \cdot (\tilde{\rho} ((\mathbf{u}_c + \mathbf{u}_{ls}) \cdot \nabla) (\mathbf{u}_c + \mathbf{u}_{ls})) = \frac{\partial}{\partial z} \left(\tilde{\rho} g \frac{\theta'_{v,c} + \theta'_{v,ls}}{\tilde{\theta}_v} \right). \quad (19)$$

Subtracting Eqs. (11)–(14) respectively from Eqs. (15)–(17) and (19) we obtain

$$\frac{\partial \mathbf{u}_c}{\partial t} + (\mathbf{u}_c \cdot \nabla) (\mathbf{u}_c + \mathbf{u}_{ls}) + (\mathbf{u}_{ls} \cdot \nabla) \mathbf{u}_c = \nabla \left(\frac{\rho'_c}{\tilde{\rho}} \right) + g \frac{\theta'_{v,c}}{\tilde{\theta}_v} \mathbf{k}, \quad (20)$$

$$\frac{\partial \theta'_c}{\partial t} + \mathbf{u}_c \cdot \nabla (\tilde{\theta} + \theta'_c + \theta'_{ls}) + \mathbf{u}_{ls} \cdot \nabla \theta'_c = \frac{\dot{Q}\theta}{c_v T}, \quad (21)$$

$$\frac{\partial q'_{v,c}}{\partial t} + \mathbf{u}_c \cdot \nabla (\tilde{q}_v + q'_{v,c} + q'_{v,ls}) + \mathbf{u}_{ls} \cdot \nabla q'_{v,c} = -S, \quad (22)$$

$$\nabla \cdot \left(\tilde{\rho} \nabla \left(\frac{\rho'_c}{\tilde{\rho}} \right) \right) + \nabla \cdot (\tilde{\rho} ((\mathbf{u}_c \cdot \nabla) (\mathbf{u}_c + \mathbf{u}_{ls}) + (\mathbf{u}_{ls} \cdot \nabla) \mathbf{u}_c)) = \frac{\partial}{\partial z} \left(\tilde{\rho} g \frac{\theta'_{v,c}}{\tilde{\theta}_v} \right). \quad (23)$$

Equations (18) and (20)–(23) form a set of governing equations used to solve for \mathbf{u}_c , ρ'_c , θ'_c , $q'_{v,c}$ and $q'_{i,c}$ in the TTL cirrus simulation.

4 Characteristics of the simulated TTL cirrus

This section describes a particular TTL cirrus simulated using our cloud resolving model. The model configuration and initial conditions of the TTL cirrus simulation are given in Sect. 4.1. The evolution of the simulated cloud is described in Sect. 4.2. Comparisons of the simulated cloud with observed TTL cirrus are discussed in Sect. 4.3.

Title Page

Abstract

Introduction

Conclusions

References

Tables

Figures

◀

▶

◀

▶

Back

Close

Full Screen / Esc

Printer-friendly Version

Interactive Discussion



4.1 Model configuration and initial conditions

The sounding for this simulation is the same as that shown in Fig. 1. The large-scale wave forcing is taken from the wave simulation described in Sect. 3.1. The horizontal domain is equal to the horizontal wavelength of the large-scale wave, which is 6000 km.

5 Periodic boundary conditions are applied at the lateral boundaries. The bottom of the domain is at $z = 15$ km and the top of the domain is at $z = 18$ km. A non-reflective open boundary condition (Bougeault, 1983; Klemp and Durran, 1983) is applied at the top and bottom of the domain. In the horizontal, the resolution is $\Delta x = 5$ km. In the vertical, Δz varies from 5 m in the proximity of the CPT at $z = 17.3$ km to 50 m at the
10 top and bottom of the domain. The time step is $\Delta t = 20$ s. The simulation is from $t = 0$ to $t = 12$ day (two wave cycles).

There is no cloud initially. A cloud forms just before $t = 2$ day in a moist region prescribed between $x = 2700$ km and 3300 km and $z = 16.8$ km and 17.3 km, which is just below the CPT. The water vapor mixing ratio q_v at the center of the moist region and outside of the moist region is respectively $2.56 \times 10^{-6} \text{ kg kg}^{-1}$ and $1.40 \times 10^{-6} \text{ kg kg}^{-1}$
15 (Fig. 4a). With respect to the base state, these values of q_v correspond to supersaturation ratios S_i of 0.5 and -0.2 at $z = 17.1$ km (the altitude at the middle of the moist region). With respect to the base state plus perturbations from the large-scale wave, S_i is 0.3 at the center of the moist region (Fig. 4b). Note that the supersaturation ratio
20 mentioned throughout this article is always with respect to ice.

The wave solution at the starting time of the cloud simulation is shown in Fig. 3¹. At this time, the moist region is experiencing positive temperature anomalies (see Fig. 4b). As the wave propagates eastward, negative temperature anomalies arrive at the moist region in about two days, at which time ice crystals are nucleated and a cloud is formed.

¹ $t = 92$ day in the large-scale wave simulation corresponds to $t = 0$ in the TTL cirrus simulation.

Title Page

Abstract

Introduction

Conclusions

References

Tables

Figures

◀

▶

◀

▶

Back

Close

Full Screen / Esc

Printer-friendly Version

Interactive Discussion



4.2 Cloud evolution

The evolution of the cloud, the supersaturation ratio, and large-scale wave temperature perturbations over the 12-day-simulation are shown in the supplement movie. In the movie, the thick, black contour marks the cloud boundary, which is defined by the 1 l^{-1} contour of ice number concentration. Filled, colored contours show the supersaturation ratios. The thin black and white contours correspond to negative and positive temperature perturbations. As shown in the movie, a cloud is formed just before $t = 2$ day. This occurs when negative temperature anomalies associated with the large-scale wave arrive at the initially prescribed moist region just below the CPT in the middle of the horizontal domain. After the initial formation stage, the cloud slowly decays as it ages but persists into the second cycle of the wave. The cloud moves about in space due to advection of water vapor and ice by the large-scale wave velocities. It also moves downward with time because of ice sedimentation.

Figures 5–7 show the time evolution of the maximum and average in space of the large-scale temperature perturbations, supersaturation ratio, ice number concentration, ice water content (IWC), radiative heating rate, and mean crystal diameter. The averages are computed over the cloudy region only (where there is ice), not over the whole spatial domain.

As shown in Fig. 5a, the amplitude of the large-scale temperature perturbations experienced by the cloud is 0.5 K on average and 1.5 K maximum. These values are consistent with the temperature anomalies experienced by TTL cirrus recorded by Immler et al. (2008, see their Fig. 4). The large-scale temperature perturbations with respect to the cloud are not perfectly sinusoidal because the cloud moves about in space and gains/loses ice over time.

During the formation of the cloud, ice nucleation followed by ice growth quickly reduces the supersaturation ratio S_i within the cloudy region from 0.6 (ice nucleation threshold) to close to zero (Fig. 5b). Throughout the cloud lifetime, ice depositional growth and sublimation maintain the average S_i within the cloud to be close zero. How-

TTL cirrus and water transport

T. Dinh et al.

Title Page

Abstract

Introduction

Conclusions

References

Tables

Figures

◀

▶

◀

▶

Back

Close

Full Screen / Esc

Printer-friendly Version

Interactive Discussion



ever, as also indicated in Fig. 5b, the minimum and maximum S_i over the cloudy region deviate from zero, indicating that some regions within the cloud are supersaturated or subsaturated.

As shown by the evolution of the ice number concentration and IWC in Figs. 6a and 6b, the cloud is formed just before $t = 2$ day. During the formation of the cloud, ice number concentration and IWC increase rapidly and obtain their maximum values just after $t = 2$ day. After the initial ice nucleation and growth, the average ice number concentration and IWC decrease quickly until day 5. At the peak of the warm phase of the wave at day 6 the cloud has become very tenuous in both ice number concentration and IWC.

As shown in Fig. 7a, the heating induced by absorption of radiation by ice crystals evolves similarly to the ice number concentration and IWC. The average radiative heating rate obtains a maximum of about 1 K d^{-1} at $t = 2.5$ day. It decreases with time after 2.5 day as ice crystals sublimate while the cloud ages. The cloud becomes very optically thin after 5 day. Between 2 day and 4 day, the absorption optical depth of the cloud is between 1×10^{-3} and 4×10^{-3} . After 5 day, the absorption optical depth decreases to very small values, on the order of 10^{-4} .

4.3 Consistency with observations

A case of observed TTL cirrus with measurements of all necessary variables to constrain model configuration is not yet available. Simultaneous measurements of environmental wind shear, temperature, relative humidity (both inside and outside cloud), as well as ice crystals size, ice number concentration and ice water content (IWC), and radiative heating rate over the cloud lifetime are required for a direct comparison with model results. Observations of the spatially and temporally varying environmental conditions in which a TTL cirrus forms and evolves are not available for any observational case study so far. Typically, current available observations provide microphysical properties, or radiative heating rate of a TTL cirrus in only a particular section of the cloud area, and at only a particular time during the lifetime of the observed cloud. Because

TTL cirrus and water transport

T. Dinh et al.

Title Page

Abstract

Introduction

Conclusions

References

Tables

Figures

◀

▶

◀

▶

Back

Close

Full Screen / Esc

Printer-friendly Version

Interactive Discussion



of this lack of detailed observations, we compare our model results to a collection of different observed TTL cirrus, rather than to any one specific observed case.

There have been observations of TTL cirrus that persist for days, a feature consistent with the cloud in our simulation. For example, during the Lidar In-space Technology Experiment (LITE), Winker and Trepte (1998) observed TTL cirrus over the same region on successive days. Recently, Taylor et al. (2011) described a TTL cirrus detected by the Cloud Aerosol Lidar and Infrared Pathfinder Satellite Observations (CALIPSO) between 27 and 29 January 2009 over the tropical Eastern Pacific. CALIPSO cannot detect clouds with optical depths smaller than 0.006 (Davis et al., 2010). Hence there is a possibility that, after 29 January 2009, the TTL cirrus reported by Taylor et al. (2011) persisted but had become too tenuous to be detected by CALIPSO. In fact, there have been in situ observations (Peter et al., 2003; Davis et al., 2010) of TTL cirrus with optical depths on the order of 10^{-4} to 10^{-3} , which is below the detection limit of CALIPSO.

The ranges between the maximum and average of the bulk properties of the cloud in our simulation, including the ice number concentration (Fig. 6a), IWC (Fig. 6b) and radiative heating rate (Fig. 7a), are within the range of observational values. The ice number concentration in TTL cirrus have been observed to vary from only a few l^{-1} (Davis et al., 2010) up to approximately $200l^{-1}$ (Lawson et al., 2008). Observed IWC ranges from just $10^{-2} \text{ mg m}^{-3}$ (Lawson et al., 2008) up to 10^2 mg m^{-3} (McFarquhar et al., 2000). The radiative heating rate could be 0.05 K d^{-1} for extremely tenuous TTL cirrus (Davis et al., 2010) up to a few K d^{-1} for optically thicker TTL cirrus (McFarquhar et al., 2000; Comstock et al., 2002; Bucholtz et al., 2010).

The average diameter of ice crystals is between $7 \mu\text{m}$ and $10 \mu\text{m}$ throughout most of our simulation (Fig. 7b). This is consistent with ice crystals of approximately $10 \mu\text{m}$ in diameter in TTL cirrus observed by Voigt et al. (2007) over Brazil, and Peter et al. (2003) over the western Indian ocean. On the other hand, Lawson et al. (2008) reported larger ice crystals with an effective diameter of approximately $18 \mu\text{m}$ for a TTL cirrus over the tropical Eastern Pacific. Nevertheless, this value is between the maximum and average sizes of ice crystals in our simulation.

TTL cirrus and water transport

T. Dinh et al.

Title Page

Abstract

Introduction

Conclusions

References

Tables

Figures

◀

▶

◀

▶

Back

Close

Full Screen / Esc

Printer-friendly Version

Interactive Discussion



TTL cirrus and water transport

T. Dinh et al.

[Title Page](#)[Abstract](#)[Introduction](#)[Conclusions](#)[References](#)[Tables](#)[Figures](#)[I◀](#)[▶I](#)[◀](#)[▶](#)[Back](#)[Close](#)[Full Screen / Esc](#)[Printer-friendly Version](#)[Interactive Discussion](#)

The ice size distributions averaged over the cloudy area in the simulation at $t = 2.5$ day, 3.5 day and 4.5 day are shown in Fig. 8a. Also plotted are the size distributions of several in-situ observed TTL cirrus. The ice size distributions of the simulated cloud agree well with in situ TTL cirrus observations for ice crystal sizes up to $20\ \mu\text{m}$. However, the number of larger ice crystals in the simulated cloud is significantly smaller than observed. Nevertheless, because the observed number of crystals larger than $20\ \mu\text{m}$ is small (note the logarithmic scale in Fig. 8a), they do not contribute significantly to the bulk properties, such as the average radiative heating rate, IWC and ice number concentration.

Larger crystals could be supported by our simulated updrafts if they had shapes other than spheres. At the same terminal fall velocity, the diameter of a spherical crystal is less than the maximum dimension of a crystal of another shape. Consider the particular TTL cirrus observed by Lawson et al. (2008), in which a few percent of crystals were plates and columns or of irregular shapes. Following these observations, suppose that 2% of the number of spherical crystals in the simulation are replaced by hexagonal plates, and an additional 1% are replaced by hexagonal columns. To calculate the sizes of plate-like and columnar crystals, we assume that they fall at the same terminal velocity as the spherical crystals that they replace. Furthermore, the aspect ratio of plate-like and columnar crystals is assumed to be 6:1, as suggested by Lawson et al. (2008)'s observations. The number concentrations of plate-like and columnar crystals are computed by ensuring conservation of the total ice mass when spherical crystals are replaced by non-spherical ones. The hypothetical size distribution of the mixed-shape crystal population (Fig. 8b) agrees well with Lawson et al. (2008)'s observations. Thus it is plausible that a better agreement between their observations and our model results can be obtained if an improved treatment of ice crystal shapes is implemented in the model.

In our hypothetical mixed-shape crystal population, almost all crystals larger than $20\ \mu\text{m}$ are non-spherical. Thus the above crystal shape argument does not apply to the TTL cirrus observed by Davis et al. (2010), in which most of the large ice crys-

TTL cirrus and water transport

T. Dinh et al.

[Title Page](#)[Abstract](#)[Introduction](#)[Conclusions](#)[References](#)[Tables](#)[Figures](#)[◀](#)[▶](#)[◀](#)[▶](#)[Back](#)[Close](#)[Full Screen / Esc](#)[Printer-friendly Version](#)[Interactive Discussion](#)

tals detected were spherical. Large spherical crystals fall much faster than the vertical velocities associated with either the equatorial Kelvin waves or the radiatively induced updrafts in our model. For example, based on Böhm (1989, Eq. 10), spherical crystals at diameters of $40\ \mu\text{m}$ and $60\ \mu\text{m}$ fall at respectively $7\ \text{cm s}^{-1}$ and $15\ \text{cm s}^{-1}$. The existence of large, spherical crystals may be explained by dynamical processes not included in the model. One possibility is the influence from the vertical motions associated with a much thicker cloud located just 2 km below the observed TTL cirrus (Davis et al., 2010, Fig. 2). In addition, large crystals may be supported against sedimentation in the presence of mesoscale gravity waves generated by nearby convective sources.

The persistence of our cloud is in contrast to that in the simulations performed by Jensen et al. (2011), who also modeled the cloud response to the mesoscale motions induced by radiative heating. In their simulations, when subject to a wind shear (vertical gradient of the horizontal wind) of $5\ \text{ms}^{-1}\ \text{km}^{-1}$, the cloud dissipated before the radiatively induced circulation could develop. The maximum shear associated with the large-scale wave in our simulation is $4.5\ \text{ms}^{-1}\ \text{km}^{-1}$ above the CPT ($z = 17.3\ \text{km}$), and $2.5\ \text{ms}^{-1}\ \text{km}^{-1}$ below this level (see Fig. 3). Since the cloud in our simulation is located below the CPT, it is subject to less shear than the cloud in Jensen et al. (2011)'s simulations. However, we argue that the spatial structure of the large-scale shear in our simulation, with larger magnitude above the CPT, is more realistic than the steady, uniform shear in Jensen et al. (2011)'s simulation. The spatially and temporally varying shear in our simulation is consistent with the z -variations of the Brunt-Väisälä frequency defined by the sounding (Fig. 1c), and the propagation of the large-scale equatorial Kelvin wave.

Another essential difference between Jensen et al. (2011)'s simulations and ours is the number of ice crystals nucleated when the cloud is formed. Jensen et al. (2011) tuned their heterogeneous nucleation scheme so that the number of ice crystals nucleated is $60\ \text{l}^{-1}$, following measurements by Lawson et al. (2008). On the other hand, homogeneous nucleation in our model produces an average number of $200\ \text{l}^{-1}$ up to a maximum of $5000\ \text{l}^{-1}$ (Fig. 6a). During formation and initial growth of the cloud, compe-

tion for available water vapor among ice crystals limits crystal sizes. In our simulation, more ice crystals are nucleated, hence sedimentation of smaller ice crystals occurs at a slower rate, which allows sufficient time for the radiatively induced dynamics to develop.

5 In situ observations of small number of ice crystals in TTL cirrus (typically less than 100 l^{-1}) have been considered as evidence against homogeneous freezing as a nucleation mechanism of ice crystals in the TTL (Jensen et al., 2010). In our simulation, although many ice crystals (on the order of 10^2 l^{-1} to 10^4 l^{-1}) nucleate homogeneously, in less than a day the number is reduced to values comparable to or smaller than
10 100 l^{-1} (Fig. 6a). The number concentration decreases due to both spreading of the cloud area and sublimation of ice crystals as they encounter dry air during sedimentation and advection in space. Hence we argue that homogeneous freezing cannot be ruled out as a viable nucleation mechanism in the TTL.

5 Transport of water vapor by the radiatively induced dynamics

15 The mesoscale circulation induced by the radiative heating (Fig. 9a) includes rising motion in the vertical column containing the cloud, subsidence to the east and west of the cloud, and horizontal inflow and outflow respectively in the lower and upper half of the cloud layer (see Fig. 10 and also Durran et al. (2009); Dinh et al. (2010)). Warming occurs in the cloud layer while cooling occurs at the top and bottom of the
20 cloud (Fig. 9b). Temperature perturbations inside the cloud are a direct result of the radiative heating, whereas temperature perturbations outside (to the east and west, above and below the cloud) are produced by radiatively induced vertical motions.

On average the rising motion within the cloud column extends above and below the levels of zero radiative heating. This behavior is shown in Figs. 11a and 11c, which
25 plot the radiative heating and its induced vertical velocity w_c at 3.5 day. Rising motion extends further above and below the cloud at earlier times (not shown). Rising motion results in adiabatic cooling just above and below the cloud (Figs. 9b and 11b). In

TTL cirrus and water transport

T. Dinh et al.

Title Page

Abstract

Introduction

Conclusions

References

Tables

Figures

◀

▶

◀

▶

Back

Close

Full Screen / Esc

Printer-friendly Version

Interactive Discussion



the layer between $z = 17.4$ km and $z = 17.6$ km, diabatic warming underlies adiabatic cooling, resulting in destabilization and convection. Convection and the convectively induced gravity waves create small-scale inhomogeneities in the cloud.

The water vapor is changed via ice depositional growth, sublimation and sedimentation, and advection of water vapor and ice by the large-scale wave and radiatively induced velocities. This change is measured as the difference in the water vapor profile between the current and the initial time. The change in the water vapor due solely to advection by the large-scale wave at the end of the simulation is negligible because this time (12 day) is a multiple of the wave period.

The water vapor mixing ratio at the end time (12 day) in the control simulation is shown in Fig. 12. The distribution of water vapor is horizontally stretched above $z = 17.2$ km and narrowed below this level. The deformation of the water vapor distribution in the horizontal direction is caused by advection by the radiatively induced horizontal velocity. Part of the initially prescribed water vapor centered at $z = 17.1$ km has been transported to above 17.2 km. This is not what we would expect from microphysical processes alone. The radiatively induced dynamics must play a significant role.

The radiative heating changes the water vapor by inducing advection of vapor and ice, and temperature perturbations T'_c . The temperature perturbations indirectly influence the transport of water vapor by affecting microphysical processes. The radiatively induced advection of vapor and of ice are respectively abbreviated as RAI and RAV. To understand the role of RAV, RAI and T'_c we consider three additional simulations, hereafter referred to as the no-RAV, no-RAV-no-RAI, and no-radiation cases. For the discussion here, the simulation described so far in this section and previously in Sect. 4, in which all relevant physical processes are resolved, is referred to as the all-physics simulation. The configuration of the test cases is the same as the all-physics simulation, except for the followings. In the no-RAV case, RAV is turned off. In the no-RAV-no-RAI case, both RAV and RAI are neglected. In the no-radiation case, the radiative heating is ignored, hence RAV, RAI and T'_c are all absent. The effects of RAV, RAI and T'_c in the water vapor transport in the vertical direction can be deduced from the horizontally

TTL cirrus and water transport

T. Dinh et al.

Title Page

Abstract

Introduction

Conclusions

References

Tables

Figures

◀

▶

◀

▶

Back

Close

Full Screen / Esc

Printer-friendly Version

Interactive Discussion



averaged changes in the water vapor densities at 12 day in the all-physics case and the three test cases (Fig. 13).

First let us examine the combined effect of RAV, RAI and T'_c by comparing the all-physics case with the no-radiation case. In the all-physics case, the region between $z = 16.85$ km and 17.15 km is dehydrated. Part of the water vapor initially in this layer has been transported downward to below 16.85 km, but most of the water vapor has been transported upward to above 17.15 km. The net direction of transport in this case is upward. In contrast, in the no-radiation case, water vapor has been removed from the initially moist layer between $z = 16.9$ km and 17.15 km and transported downward into the layer below. Downward transport of water vapor occurs as ice crystals are nucleated, grow and then sediment to the subsaturated region below, where they sublimate and return water vapor to the air. The difference between the all-physics and no-radiation cases indicates that together T'_c , RAI, and RAV lead to upward transport of water vapor, counteracting and overwhelming downward transport due to microphysical processes.

Now consider the individual effects of RAV, RAI and T'_c . First, the direction of transport associated with RAV can be deduced by comparing the all-physics case with the no-RAV case. As seen in Fig. 13, the direction of transport is upward in the all-physics case and downward in the no-RAV case. This indicates that RAV is the primary cause for the upward transport of water vapor and that RAI and T'_c play only secondary roles. Next, the direction of transport associated with RAI can be deduced by comparing the no-RAV case with the no-RAV-no-RAI case. There is an enhancement of dehydration above 17.0 km and an increase in net downward transport in the no-RAV case compared with the no-RAV-no-RAI case. RAI enhances convective mixing of ice crystals with the air at the top margin of the original moist patch, thereby enhancing the deposition of water vapor onto the ice crystals there. Furthermore, within the cloud the radiatively induced updraft partially offsets sedimentation, causing ice to fall more slowly to the dry air below. This gives crystals slightly more time to persist and use up more water vapor in depositional growth. Finally, the direction of transport associated with

TTL cirrus and water transport

T. Dinh et al.

[Title Page](#)[Abstract](#)[Introduction](#)[Conclusions](#)[References](#)[Tables](#)[Figures](#)[◀](#)[▶](#)[◀](#)[▶](#)[Back](#)[Close](#)[Full Screen / Esc](#)[Printer-friendly Version](#)[Interactive Discussion](#)

T'_c can be deduced by comparing the no-RAV-no-RAI case with the no-radiation case. There is a reduction in dehydration between 17.0 km and 17.1 km and a decrease in net downward transport in the no-RAV-no-RAI case compared with the no-radiation case. The diabatic warming (see Fig. 9b) reduces the relative humidity, hence ice deposi-
5 tional growth within the cloud. Ice depositional growth followed by ice sedimentation results in downward transport of water vapor. Hence, via their interactions with ice depositional growth, RAI and T'_c indirectly transport water vapor respectively downward and upward. The directions of transport induced by T'_c , RAI, RAV, and microphysical processes are summarized in Table 1.

10 In contrast to RAI and T'_c , RAV plays a primary and direct role in the transport of water vapor. The significance of RAV compared with either RAI or T'_c is confirmed by the difference between the all-physics case and the no-radiation case, which is much more significant than that between either the no-RAV case or the no-RAI-no-RAI case and the no-radiation case. When RAV is present, the radiatively induced updraft advects
15 the water vapor contained in the cloudy air upwards. This leads to upward transport of water vapor because the cloudy air is approximately at saturation throughout the cloud lifetime (see Fig. 5b) and contains more water vapor than the environment. RAV is much more effective than RAI at upward transport of water because, unlike ice crystals, water vapor does not sediment. RAI cannot transport ice upward since, on average, the radiatively induced updraft w_c is smaller than ice sedimentation speed V_t . For
20 example, at 3.5 day, w_c within the cloud is less than 2 mm s^{-1} (see Fig. 11c), whereas V_t is 4.5 mm s^{-1} for a crystal with $5 \mu\text{m}$ radius.

25 Similarly to RAI, RAV also indirectly induces downward transport of water vapor by enhancing ice depositional growth. This indirect, downward transport of water vapor induced by RAV is much less significant than its direct, upward transport. Nevertheless, the enhancement of ice depositional growth by RAV reduces the overall rate of cloud dissipation and is important for the persistence of the cloud. As explained by Dinh et al. (2010), the horizontal velocity u_c induces horizontal influx of air and water vapor into the lower half of the cloud. Accompanied with upward advection by w_c within the cloud,

TTL cirrus and water transport

T. Dinh et al.

Title Page

Abstract

Introduction

Conclusions

References

Tables

Figures

◀

▶

◀

▶

Back

Close

Full Screen / Esc

Printer-friendly Version

Interactive Discussion



this results in water vapor flux convergence and ice depositional growth. As shown in Fig. 14, in the upper half of the cloud, there is considerably more positive latent heat release, i.e. ice growth, in the all-physics case than in the no-RAV case. In the all-physics case, the rate of change in q_v due to vertical advection within the cloud is $-w_c \frac{\partial q_v}{\partial z}$, where $w_c > 0$ and $\frac{\partial q_v}{\partial z} < 0$ for $z > 17.1$ km (see Fig. 11d). This means that upward advection of water vapor increases q_v and favors ice growth above 17.1 km.

6 Conclusions

We have performed two-dimensional simulations of TTL cirrus under the influence of a large-scale equatorial Kelvin wave. The bulk radiative and microphysical properties (radiative heating rate, IWC and ice number concentration) of the simulated cloud agree reasonably well with observations. However, our current simplified model, which assumes that all crystals are spherical, does not reproduce crystals larger than $20 \mu\text{m}$. Ice crystals of such large sizes have been reported in several observational field campaigns. Hypothetically, if three percent of the spherical crystals in the model output were replaced by non-spherical crystals, we would be able to explain reasonably well the existence of crystals larger than $20 \mu\text{m}$. Nevertheless, the number of these large ice crystals is small, so they do not contribute significantly to the bulk properties of the cloud.

In the model, the large-scale wave is considered as an external forcing on the cloud. In other words, the wave influences the cloud processes, but the cloud processes do not change the wave. The large-scale wave exerts realistic spatially and temporally varying shear and temperature perturbations on the cloud. During the cold phase of the wave, ice crystals nucleate and grow. During the warm phase of the wave, the cloud attenuates but may not dissipate completely.

In addition to perturbations associated with the large-scale wave, cloud microphysical processes are influenced by the dynamics induced by the radiative heating. The radiative heating in TTL cirrus results from the absorption of radiation by ice crystals.

Title Page

Abstract

Introduction

Conclusions

References

Tables

Figures

◀

▶

◀

▶

Back

Close

Full Screen / Esc

Printer-friendly Version

Interactive Discussion



TTL cirrus and water transport

T. Dinh et al.

[Title Page](#)[Abstract](#)[Introduction](#)[Conclusions](#)[References](#)[Tables](#)[Figures](#)[◀](#)[▶](#)[◀](#)[▶](#)[Back](#)[Close](#)[Full Screen / Esc](#)[Printer-friendly Version](#)[Interactive Discussion](#)

The mesoscale circulation induced by the radiative heating consists of rising motion in the vertical column containing the cloud, subsidence to the east and west of the cloud, and horizontal inflow and outflow respectively in the lower and upper half of the cloud layer. In addition, the radiative heating causes instability and convection at the cloud top. This results in mixing with the environmental air at the cloud top and small-scale inhomogeneities in the cloud.

In TTL cirrus, both microphysical and dynamical processes contribute to transport of water vapor in the vertical direction. Ice nucleation and depositional growth, followed by sedimentation and sublimation, lead to downward transport of water vapor. On the other hand, the radiatively induced mesoscale circulation induces upward advection of the cloudy air. When the surrounding air is drier than the cloudy air, upward advection of the cloudy air is equivalent to upward transport of water vapor. Under the conditions specific to our simulations, the radiatively induced upward transport of water vapor dominates over the downward transport by microphysical processes. The net result is upward transport of water vapor, which is equivalent to hydration of the lower stratosphere.

There are continuous interactions between the cloudy air and the environmental air at all sides of the cloud: at the cloud base as ice falls relative to the air, at the cloud top via convective mixing, and at the lateral sides of the cloud by horizontal advection. Hence cloud processes and the transport of water vapor are sensitive to the relative humidity of the air surrounding the cloud. The sensitivity of model results to the relative humidity of the surrounding air will be discussed in a subsequent paper. There we will show that, in contrast to the cases presented here, when the air surrounding the cloud contains more water vapor than the cloudy air, the mesoscale circulation enhances ice depositional growth and works in concert with microphysical processes to produce downward transport of water vapor.

We have demonstrated the importance of the radiatively induced mesoscale dynamics in TTL cirrus with a maximum radiative heating rate of about 1 K d^{-1} . For a stronger heating rate, the effect of the mesoscale dynamics in the vertical transport of water va-

por would be more significant. TTL cirrus with a radiative heating rate of about 3 K d^{-1} have been observed, either by ground-based lidar (Comstock et al., 2002), or directly during flights through the cloud (Bucholtz et al., 2010). Unfortunately these cases are not accompanied by observations of ice crystal size and concentration. Observations of the microphysical properties would help to constrain the model simulations and quantify the dehydration impact of these optically thicker TTL cirrus cases.

Acknowledgements. This research was supported by NSF grant ATM-0926996. We would like to thank Dr. Marat Khairoutdinov for sharing the System of Atmospheric Modeling model with our group.

References

- Bannon, P. R.: Theoretical foundations for models of moist convection, *J. Atmos. Sci.*, 59, 1967–1982, 2002. 10733
- Blossey, P. N. and Durran, D. R.: Selective monotonicity preservation in scalar advection, *J. Comp. Phys.*, 227, 5160–5183, 2008. 10734
- Boehm, M. T. and Verlinde, J.: Stratospheric influence on upper tropospheric tropical cirrus, *Geophys. Res. Lett.*, 27, 3209–3212, 2000. 10731, 10735, 10739
- Böhm, H. P.: A general equation for the terminal fall speed of solid hydrometeors, *J. Atmos. Sci.*, 46, 2419–2427, 1989. 10735, 10747
- Bougeault, P.: A non-reflective upper boundary condition for limited-height hydrostatic models, *Mon. Weather Rev.*, 111, 420–429, 1983. 10738, 10742
- Brewer, A. W.: Evidence for a world circulation provided by the measurements of helium and water vapour distribution in the stratosphere, *Q. J. Roy. Meteor. Soc.*, 75, 351–363, 1949. 10730
- Bucholtz, A., Hlavka, D. L., McGill, M. J., Schmidt, K. S., Pilewskie, P., Davis, S. M., Reid, E. A., and Walker, A. L.: Directly measured heating rates of a tropical subvisible cirrus cloud, *J. Geophys. Res.*, 115, D00J09, doi:10.1029/2009JD013128, 2010. 10732, 10745, 10754
- Chen, J. P. and Lamb, D.: Simulation of cloud microphysical and chemical processes using a multicomponent framework. Part I: Description of the microphysical model, *J. Atmos. Sci.*, 51, 2613–2613, 1994. 10735

TTL cirrus and water transport

T. Dinh et al.

Title Page

Abstract

Introduction

Conclusions

References

Tables

Figures

◀

▶

◀

▶

Back

Close

Full Screen / Esc

Printer-friendly Version

Interactive Discussion



- Comstock, J. M., Ackerman, T. P., and Mace, G. G.: Ground-based lidar and radar remote sensing of tropical cirrus clouds at Nauru Island: Cloud statistics and radiative impacts, *J. Geophys. Res.*, 107, 4714, doi:10.1029/2002JD002203, 2002. 10732, 10745, 10754
- Davis, S., Hlavka, D., Jensen, E., Rosenlof, K., Yang, Q., Schmidt, S., Borrmann, S., Frey, W., Lawson, P., Voemel, H., and Bui, T. P.: In situ and lidar observations of tropopause subvisible cirrus clouds during TC4, *J. Geophys. Res.*, 115, D00J17, doi:10.1029/2009JD013093, 2010. 10745, 10746, 10747, 10767
- Dinh, T. and Durran, D. R.: A hybrid bin scheme to solve the condensation/evaporation equation using a cubic distribution function, *Atmos. Chem. Phys.*, 12, 1003–1011, doi:10.5194/acp-12-1003-2012, 2012. 10735
- Dinh, T., Durran, D. R., and Ackerman, T.: Maintenance of tropical tropopause layer cirrus, *J. Geophys. Res.*, 115, D02104, doi:10.1029/2009JD012735, 2010. 10732, 10735, 10748, 10751
- Durran, D. R., Dinh, T., Ammerman, M., and Ackerman, T.: The mesoscale dynamics of thin tropical tropopause cirrus, *J. Atmos. Sci.*, 66, 2859–2873, doi:10.1175/2009JAS3046.1, 2009. 10732, 10734, 10748
- Fujiwara, M., Iwasaki, S., Shimizu, A., Inai, Y., Shiotani, M., Hasebe, F., Matsui, I., Sugimoto, N., Okamoto, H., Nishi, N., Hamada, A., Sakazaki, T., and Yoneyama, K.: Cirrus observations in the tropical tropopause layer over the western Pacific, *J. Geophys. Res.*, 114, D9304, doi:10.1029/2008JD011040, 2009. 10731, 10735
- Haladay, T. and Stephens, G.: Characteristics of tropical thin cirrus clouds deduced from joint CloudSat and CALIPSO observations, *J. Geophys. Res.*, 114, D00A25, doi:10.1029/2008JD010675, 2009. 10732
- Hartmann, D. L., Holton, J. R., and Fu, Q.: The heat balance of the tropical tropopause, cirrus, and stratospheric dehydration, *Geophys. Res. Lett.*, 28, 1969–1972, doi:10.1029/2000GL012833, 2001. 10732
- Holton, J. R. and Gettelman, A.: Horizontal transport and the dehydration of the stratosphere, *Geophys. Res. Lett.*, 28, 2799–2802, 2001. 10731, 10732
- Immler, F., Krüger, K., Fujiwara, M., Verver, G., Rex, M., and Schrems, O.: Correlation between equatorial Kelvin waves and the occurrence of extremely thin ice clouds at the tropical tropopause, *Atmos. Chem. Phys.*, 8, 4019–4026, doi:10.5194/acp-8-4019-2008, 2008. 10731, 10735, 10739, 10743

TTL cirrus and water transport

T. Dinh et al.

[Title Page](#)[Abstract](#)[Introduction](#)[Conclusions](#)[References](#)[Tables](#)[Figures](#)[◀](#)[▶](#)[◀](#)[▶](#)[Back](#)[Close](#)[Full Screen / Esc](#)[Printer-friendly Version](#)[Interactive Discussion](#)

TTL cirrus and water transport

T. Dinh et al.

[Title Page](#)[Abstract](#)[Introduction](#)[Conclusions](#)[References](#)[Tables](#)[Figures](#)[◀](#)[▶](#)[◀](#)[▶](#)[Back](#)[Close](#)[Full Screen / Esc](#)[Printer-friendly Version](#)[Interactive Discussion](#)

- Jensen, E. and Pfister, L.: Transport and freeze-drying in the tropical tropopause layer, *J. Geophys. Res.*, 109, D02207, 2004. 10732
- Jensen, E. J., Toon, O. B., Pfister, L., and Selkirk, H. B.: Dehydration of the upper troposphere and lower stratosphere by subvisible cirrus clouds near the tropical tropopause, *Geophys. Res. Lett.*, 23, 825–828, 1996. 10732
- Jensen, E. J., Pfister, L., Ackerman, A. S., and Tabazadeh, A.: A conceptual model of the dehydration of air due to freeze-drying by optically thin, laminar cirrus rising slowly across the tropical tropopause, *J. Geophys. Res.*, 106, 17237–17252, 2001. 10732, 10735
- Jensen, E. J., Pfister, L., Bui, T.-P., Lawson, P., and Baumgardner, D.: Ice nucleation and cloud microphysical properties in tropical tropopause layer cirrus, *Atmos. Chem. Phys.*, 10, 1369–1384, doi:10.5194/acp-10-1369-2010, 2010. 10748
- Jensen, E. J., Pfister, L., and Toon, O. B.: Impact of radiative heating, wind shear, temperature variability, and microphysical processes on the structure and evolution of thin cirrus in the tropical tropopause layer, *J. Geophys. Res.*, 116, D12209, doi:10.1029/2010JD015417, 2011. 10732, 10747
- Kay, J. E. and Wood, R.: Timescale analysis of aerosol sensitivity during homogeneous freezing and implications for upper tropospheric water vapor budgets, *Geophys. Res. Lett.*, 35, L10809, doi:10.1029/2007GL032628, 2008. 10735
- Khairoutdinov, M. F. and Randall, D. A.: Cloud resolving modeling of the ARM summer 1997 IOP: Model formulation, results, uncertainties, and sensitivities., *J. Atmos. Sci.*, 60, 607–625, 2003. 10734
- Klemp, J. B. and Durran, D. R.: An upper boundary condition permitting internal gravity wave radiation in numerical mesoscale models, *Mon. Weather Rev.*, 111, 430–444, 1983. 10738, 10742
- Koop, T., Luo, B., Tsias, A., and Peter, T.: Water activity as the determinant for homogeneous ice nucleation in aqueous solutions, *Nature*, 406, 611–614, 2000. 10735
- Lawson, R. P., Pilon, B., Baker, B., Mo, Q., Jensen, E., Pfister, L., and Bui, P.: Aircraft measurements of microphysical properties of subvisible cirrus in the tropical tropopause layer, *Atmos. Chem. Phys.*, 8, 1609–1620, doi:10.5194/acp-8-1609-2008, 2008. 10731, 10745, 10746, 10747, 10767
- Mace, G. G., Zhang, Q., Vaughan, M., Marchand, R., Stephens, G., Trepte, C., and Winker, D.: A description of hydrometeor layer occurrence statistics derived from the first year of merged Cloudsat and CALIPSO data, *J. Geophys. Res.*, 114, D8, 2009. 10731

TTL cirrus and water transport

T. Dinh et al.

[Title Page](#)[Abstract](#)[Introduction](#)[Conclusions](#)[References](#)[Tables](#)[Figures](#)[◀](#)[▶](#)[◀](#)[▶](#)[Back](#)[Close](#)[Full Screen / Esc](#)[Printer-friendly Version](#)[Interactive Discussion](#)

- Magee, N., Moyle, A. M., and Lamb, D.: Experimental determination of the deposition coefficient of small cirrus-like ice crystals near -50°C , *Geophys. Res. Lett.*, 33, L17813, doi:10.1029/2006GL026665, 2006. 10735
- Massie, S., Gettelman, A., Randel, W., and Baumgardner, D.: Distribution of tropical cirrus in relation to convection, *J. Geophys. Res.*, 107, doi:10.1029/2001JD001293, 2002. 10731
- McFarquhar, G. M., Heymsfield, A. J., Spinhirne, J., and Hart, B.: Thin and subvisual tropopause tropical cirrus: Observations and radiative impacts, *J. Atmos. Sci.*, 57, 1841–1853, 2000. 10732, 10745, 10767
- Peter, T., Luo, B. P., Wirth, M., Kiemle, C., Flentje, H., Yushkov, V. A., Khattatov, V., Rudakov, V., Thomas, A., Borrmann, S., Toci, G., Mazzinghi, P., Beuermann, J., Schiller, C., Cairo, F., Di Donfrancesco, G., Adriani, A., Volk, C. M., Strom, J., and Noone, K.: Ultrathin tropical tropopause clouds (UTTCs): I. Cloud morphology and occurrence, *Atmos. Chem. Phys.*, 3, 1083–1091, doi:10.5194/acp-3-1083-2003, 2003. 10731, 10745
- Rosenfield, J. E., Considine, D. B., Schoeberl, M., and Browell, E.: The impact of subvisible cirrus clouds near the tropical tropopause on stratospheric water vapor, *Geophys. Res. Lett.*, 25, 1883–1886, doi:10.1029/98GL01294, 1998. 10732
- Taylor, J. R., Randel, W. J., and Jensen, E. J.: Cirrus cloud-temperature interactions in the tropical tropopause layer: a case study, *Atmos. Chem. Phys.*, 11, 10085–10095, doi:10.5194/acp-11-10085-2011, 2011. 10731, 10745
- Thomas, A., Borrmann, S., Kiemle, C., Cairo, F., Volk, M., Beuermann, J., Lepuchov, B., Santacesaria, V., Matthey, R., Rudakov, V., Yushkov, V., MacKenzie, A. R., and Stefanutti, L.: In situ measurements of background aerosol and subvisible cirrus in the tropical tropopause region, *J. Geophys. Res.*, 107, 4763, doi:10.1029/2001JD001385, 2002. 10731
- Virts, K. S. and Wallace, J. M.: Annual, interannual, and intraseasonal variability of tropical tropopause transition layer cirrus, *J. Atmos. Sci.*, 67, 3097–3112, 2010. 10731
- Voigt, C., Karcher, B., Schlager, H., Schiller, C., Kramer, M., de Reus, M., Vossing, H., Borrmann, S., and Mitev, V.: In-situ observations and modeling of small nitric acid-containing ice crystals, *Atmos. Chem. Phys.*, 7, 3373–3383, doi:10.5194/acp-7-3373-2007, 2007. 10745, 10767
- Wang, P.-H., Minnis, P., McCormick, M. P., Kent, G. S., and Skeens, K. M.: A 6-year climatology of cloud occurrence frequency from Stratospheric Aerosol and Gas Experiment II observations (1985–1990), *J. Geophys. Res.*, 101, 29407–29429, 1996. 10731

Winker, D. M. and Trepte, C. R.: Laminar cirrus observed near the tropical tropopause by LITE, Geophys. Res. Lett., 25, 3351–3354, 1998. 10731, 10745
Yang, Q., Fu, Q., and Hu, Y.: Radiative impacts of clouds in the tropical tropopause layer, J. Geophys. Res., 115, D00H12, doi:10.1029/2009JD012393, 2010. 10732

TTL cirrus and water transport

T. Dinh et al.

[Title Page](#)

[Abstract](#)

[Introduction](#)

[Conclusions](#)

[References](#)

[Tables](#)

[Figures](#)

[I◀](#)

[▶I](#)

[◀](#)

[▶](#)

[Back](#)

[Close](#)

[Full Screen / Esc](#)

[Printer-friendly Version](#)

[Interactive Discussion](#)



TTL cirrus and water transport

T. Dinh et al.

[Title Page](#)[Abstract](#)[Introduction](#)[Conclusions](#)[References](#)[Tables](#)[Figures](#)[I◀](#)[▶I](#)[◀](#)[▶](#)[Back](#)[Close](#)[Full Screen / Esc](#)[Printer-friendly Version](#)[Interactive Discussion](#)**Table 1.** Directions of water vapor transport induced by microphysical processes and the radiatively induced temperature perturbations, advection of ice, and advection of water vapor.

Microphysics and radiatively induced processes	up
Ice depositional growth, followed by sedimentation	down
All radiatively induced processes	up
Radiatively induced advection of vapor	up
Radiatively induced advection of ice	down
Radiatively induced temperature perturbations	up

TTL cirrus and water transport

T. Dinh et al.

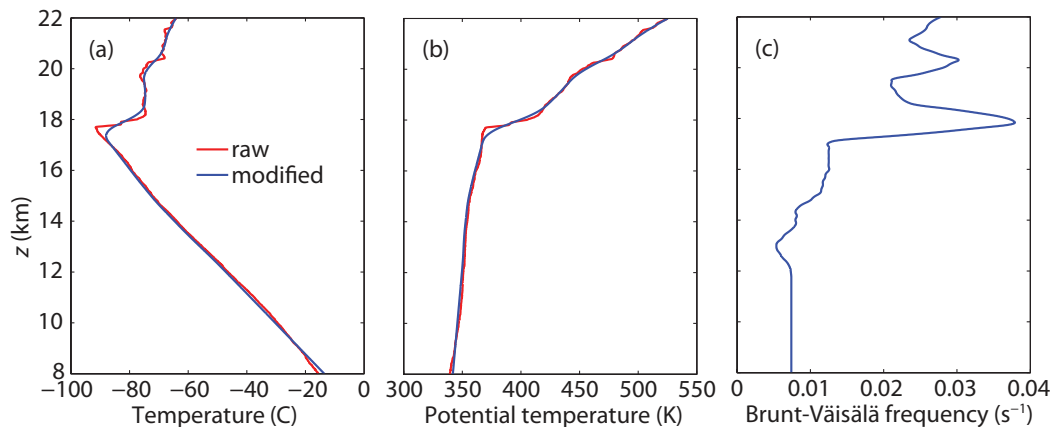


Fig. 1. Temperature (a) and potential temperature (b) of the raw and modified soundings, and the Brunt-Väisälä frequency (c) of the modified sounding.

[Title Page](#)[Abstract](#)[Introduction](#)[Conclusions](#)[References](#)[Tables](#)[Figures](#)[◀](#)[▶](#)[◀](#)[▶](#)[Back](#)[Close](#)[Full Screen / Esc](#)[Printer-friendly Version](#)[Interactive Discussion](#)

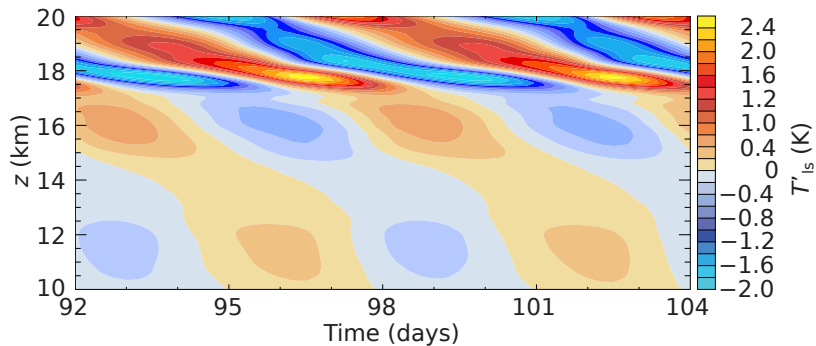


Fig. 2. Wave temperature perturbations at $x = 3000$ km (middle of the domain) as a function of time and altitude.

TTL cirrus and water transport

T. Dinh et al.

Title Page	
Abstract	Introduction
Conclusions	References
Tables	Figures
◀	▶
◀	▶
Back	Close
Full Screen / Esc	
Printer-friendly Version	
Interactive Discussion	



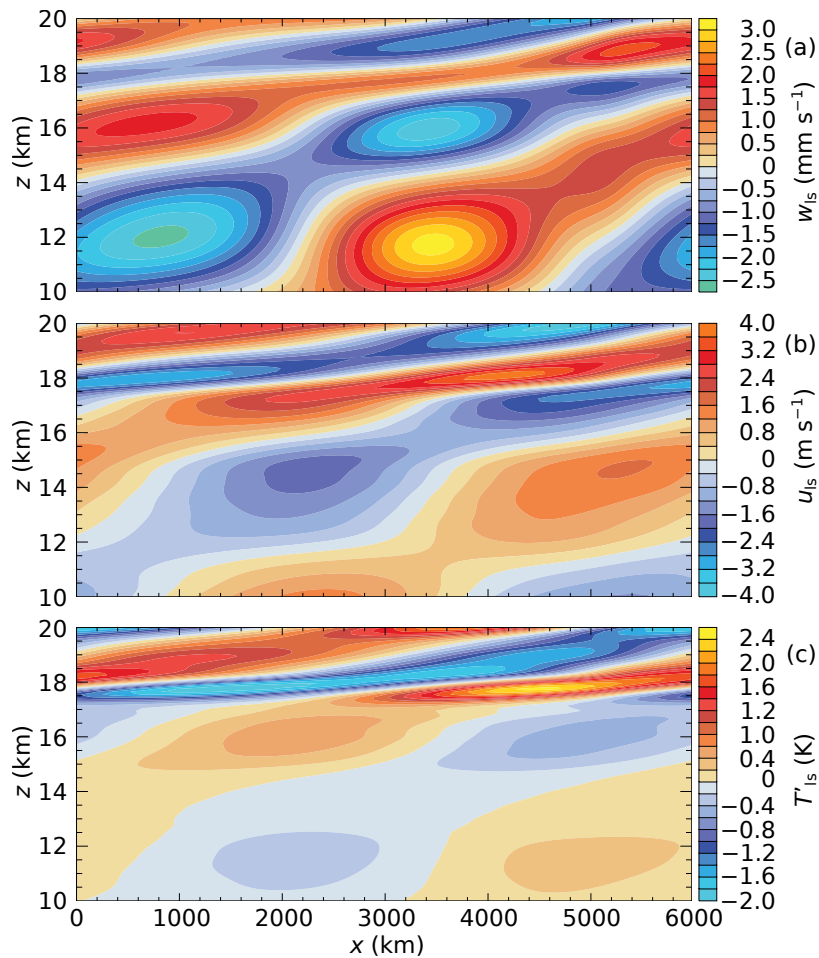


Fig. 3. Wave vertical velocity **(a)**, horizontal velocity **(b)**, and temperature perturbations **(c)** at 92 day.

TTL cirrus and water transport

T. Dinh et al.

Title Page	
Abstract	Introduction
Conclusions	References
Tables	Figures
◀	▶
◀	▶
Back	Close
Full Screen / Esc	
Printer-friendly Version	
Interactive Discussion	



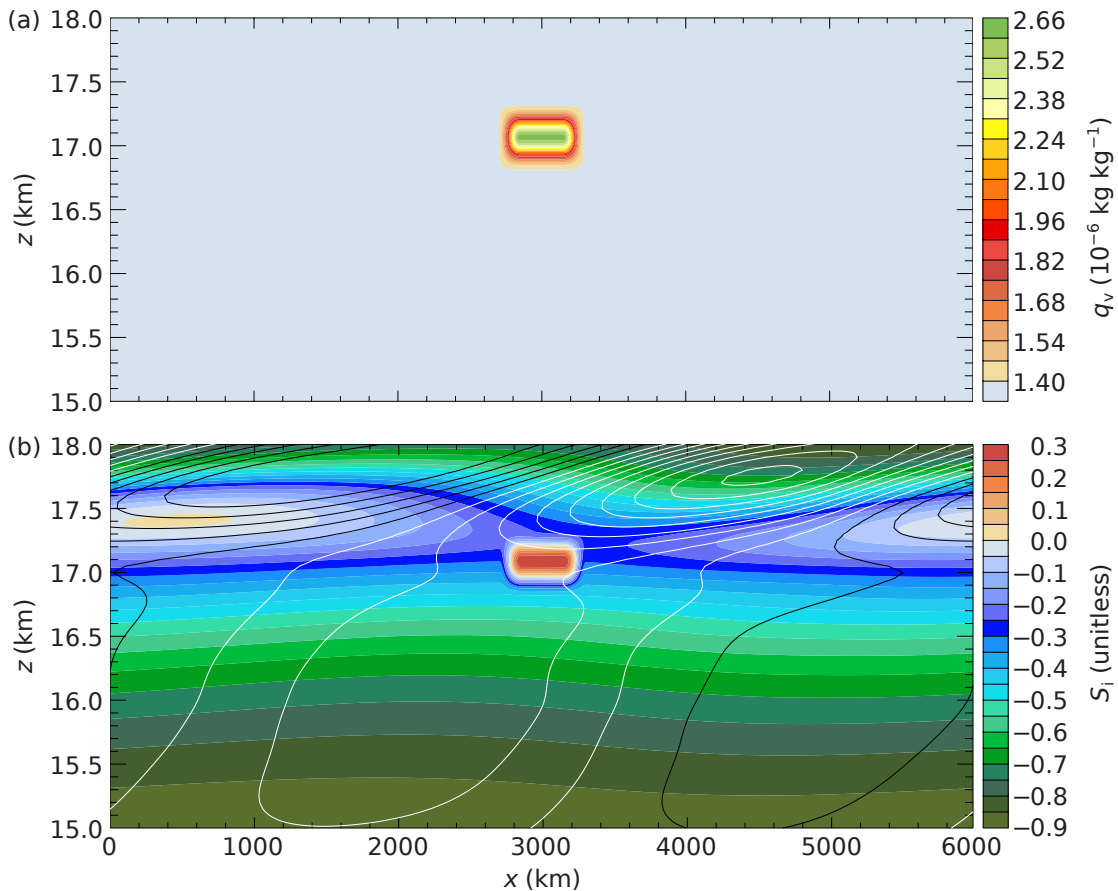


Fig. 4. Water vapor mixing ratio **(a)** and supersaturation ratio **(b)** at the initial time. In **(b)**, the black and white contours respectively show negative and positive large-scale temperature perturbations.

TTL cirrus and water transport

T. Dinh et al.

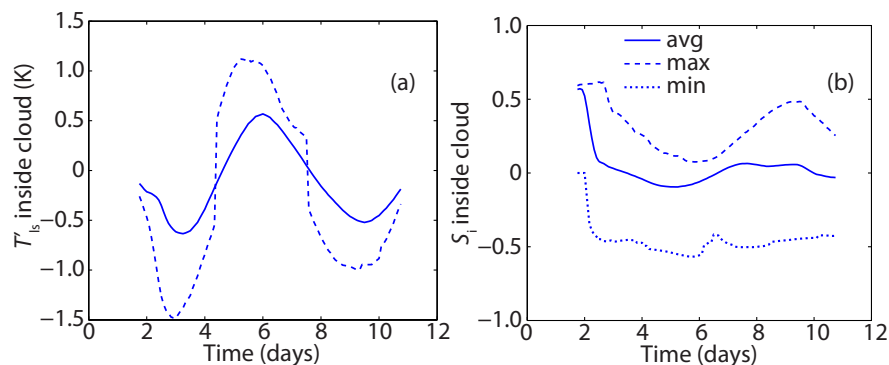


Fig. 5. Time evolution of the maximum and average over the cloudy region of the large-scale temperature perturbations **(a)** and supersaturation ratio **(b)**. In **(b)** the minimum over the cloudy region of the supersaturation ratio is also shown.

[Title Page](#)[Abstract](#)[Introduction](#)[Conclusions](#)[References](#)[Tables](#)[Figures](#)[◀](#)[▶](#)[◀](#)[▶](#)[Back](#)[Close](#)[Full Screen / Esc](#)[Printer-friendly Version](#)[Interactive Discussion](#)

TTL cirrus and water transport

T. Dinh et al.

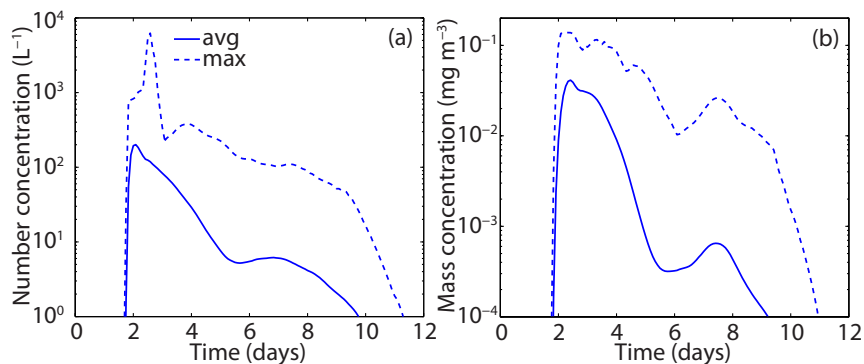


Fig. 6. Same as Fig. 5 but for ice number concentration (a) and IWC (b). Ice number concentration and IWC are shown in logarithmic scale.

[Title Page](#)[Abstract](#)[Introduction](#)[Conclusions](#)[References](#)[Tables](#)[Figures](#)[◀](#)[▶](#)[◀](#)[▶](#)[Back](#)[Close](#)[Full Screen / Esc](#)[Printer-friendly Version](#)[Interactive Discussion](#)

TTL cirrus and water transport

T. Dinh et al.

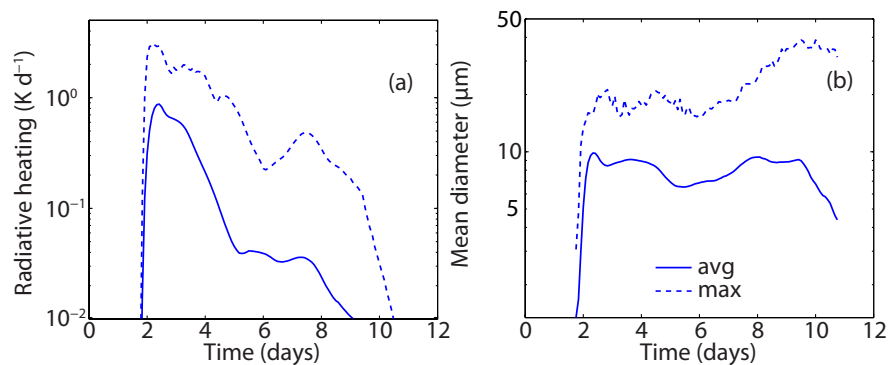


Fig. 7. Same as Fig. 5 but for radiative heating rate **(a)** and mean diameter of ice crystals **(b)**. Radiative heating rate and mean diameter are shown in logarithmic scale.

[Title Page](#)[Abstract](#)[Introduction](#)[Conclusions](#)[References](#)[Tables](#)[Figures](#)[◀](#)[▶](#)[◀](#)[▶](#)[Back](#)[Close](#)[Full Screen / Esc](#)[Printer-friendly Version](#)[Interactive Discussion](#)

TTL cirrus and water transport

T. Dinh et al.

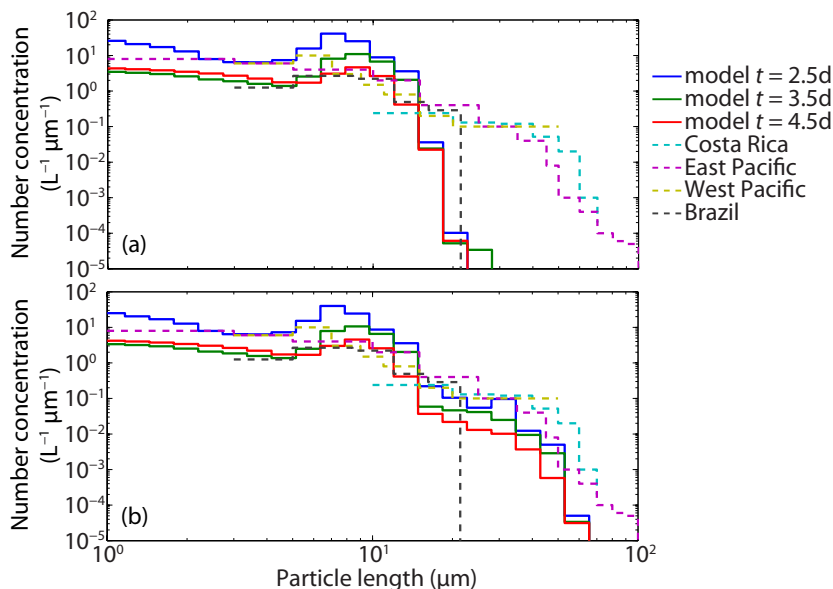


Fig. 8. Ice number size distributions from model at 2.5 day, 3.5 day and 4.5 day, and observations in TTL cirrus over Costa Rica (Davis et al., 2010), East Pacific (Lawson et al., 2008), West Pacific (McFarquhar et al., 2000) and Brazil (Voigt et al., 2007). In **(a)**, all ice crystals in the simulated cloud are spheres, as assumed in the bin microphysics and radiation schemes in the model. In **(b)**, 2% and 1% of spherical crystals in the model output are replaced respectively by plate-like and columnar crystals.

Title Page

Abstract

Introduction

Conclusions

References

Tables

Figures

◀

▶

◀

▶

Back

Close

Full Screen / Esc

Printer-friendly Version

Interactive Discussion



TTL cirrus and water transport

T. Dinh et al.

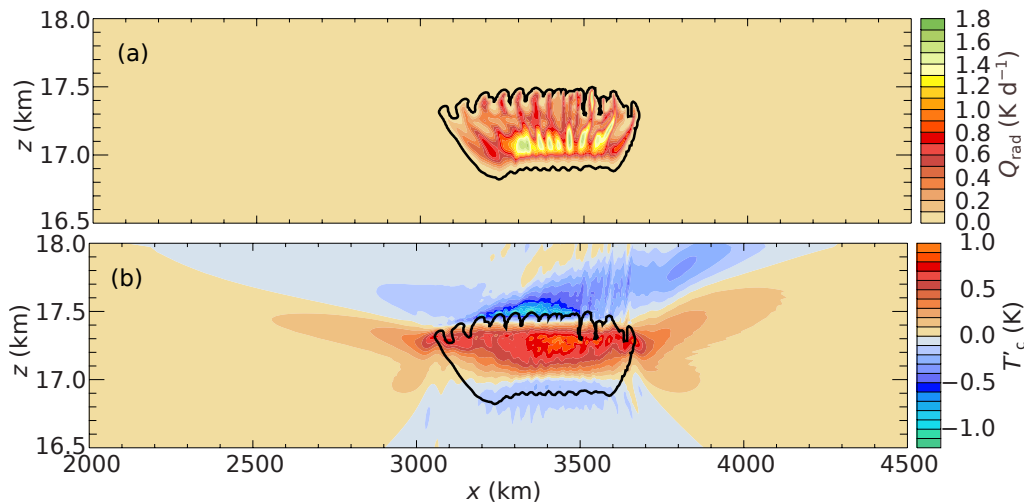


Fig. 9. The radiative heating **(a)** and induced temperature perturbations **(b)** at 3.5 day. The black outline in each figure marks the radiative heating rate contour of 0.01 K d^{-1} . Note the ratio of horizontal to vertical scales is 10^4 to 6.

Title Page

Abstract

Introduction

Conclusions

References

Tables

Figures

◀

▶

◀

▶

Back

Close

Full Screen / Esc

Printer-friendly Version

Interactive Discussion



TTL cirrus and water transport

T. Dinh et al.

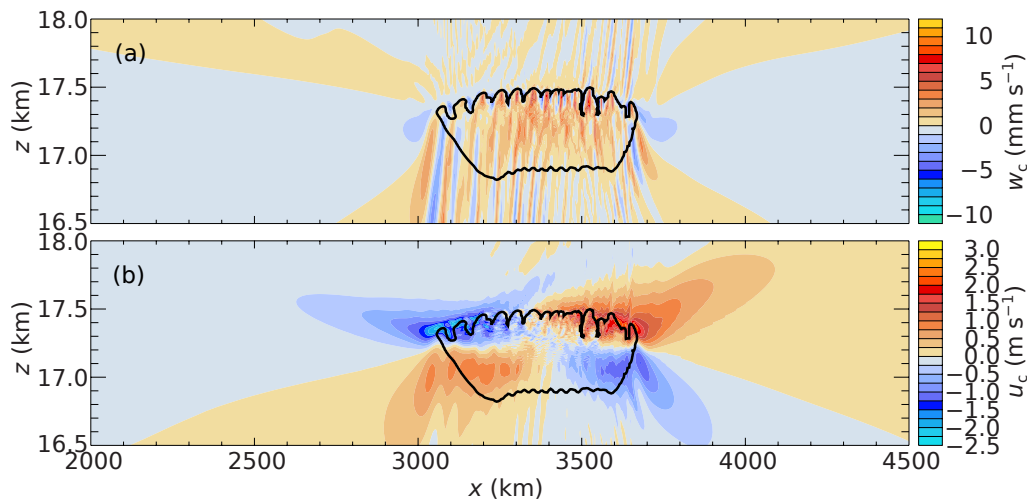


Fig. 10. Same as Fig. 9 but for the radiatively induced vertical velocity **(a)** and horizontal velocity **(b)**.

[Title Page](#)[Abstract](#)[Introduction](#)[Conclusions](#)[References](#)[Tables](#)[Figures](#)[◀](#)[▶](#)[◀](#)[▶](#)[Back](#)[Close](#)[Full Screen / Esc](#)[Printer-friendly Version](#)[Interactive Discussion](#)

TTL cirrus and water transport

T. Dinh et al.

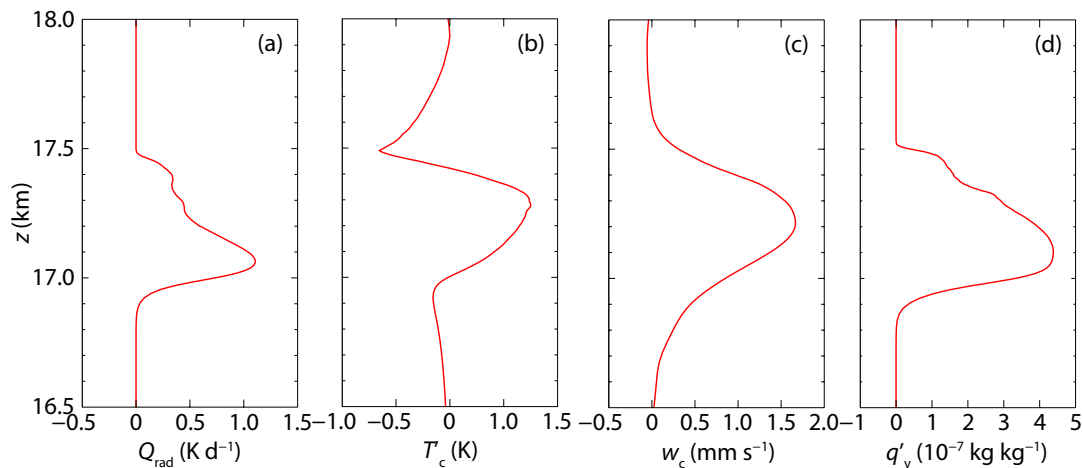


Fig. 11. Horizontal averages between $x = 3200$ km and 3600 km of the radiative heating rate **(a)**, its induced temperature perturbations **(b)**, its induced vertical velocity **(c)**, and perturbation water vapor mixing ratio **(d)** at 3.5 day.

[Title Page](#)[Abstract](#)[Introduction](#)[Conclusions](#)[References](#)[Tables](#)[Figures](#)[◀](#)[▶](#)[◀](#)[▶](#)[Back](#)[Close](#)[Full Screen / Esc](#)[Printer-friendly Version](#)[Interactive Discussion](#)

TTL cirrus and water transport

T. Dinh et al.

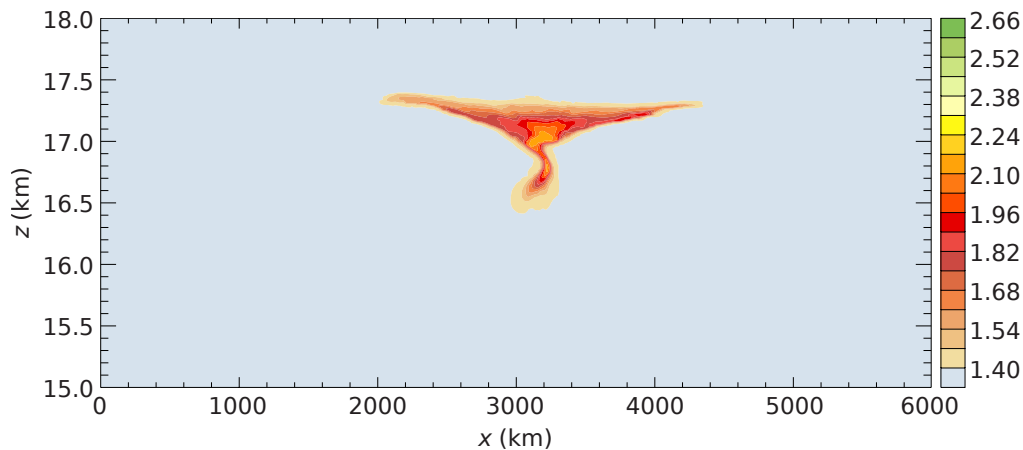


Fig. 12. Water vapor mixing ratio ($10^{-6} \text{ kg kg}^{-1}$) at the final time in the control simulation.

[Title Page](#)[Abstract](#)[Introduction](#)[Conclusions](#)[References](#)[Tables](#)[Figures](#)[I◀](#)[▶I](#)[◀](#)[▶](#)[Back](#)[Close](#)[Full Screen / Esc](#)[Printer-friendly Version](#)[Interactive Discussion](#)

TTL cirrus and water transport

T. Dinh et al.

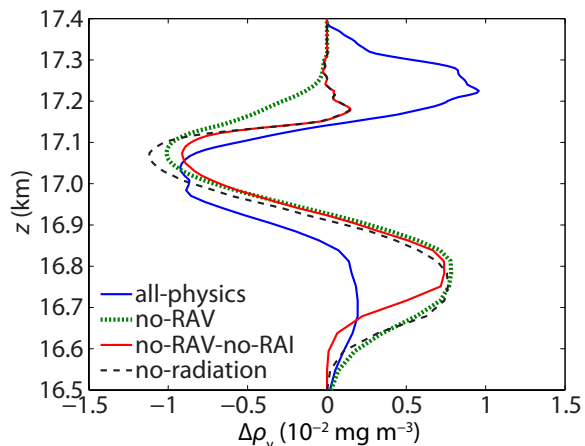


Fig. 13. Differences in the water vapor densities between the final and initial time averaged over the horizontal domain. Results are shown for four simulations: all-physics, no-RAV, no-RAV-no-RAI, and no-radiation.

Title Page

Abstract

Introduction

Conclusions

References

Tables

Figures

◀

▶

◀

▶

Back

Close

Full Screen / Esc

Printer-friendly Version

Interactive Discussion



TTL cirrus and water transport

T. Dinh et al.

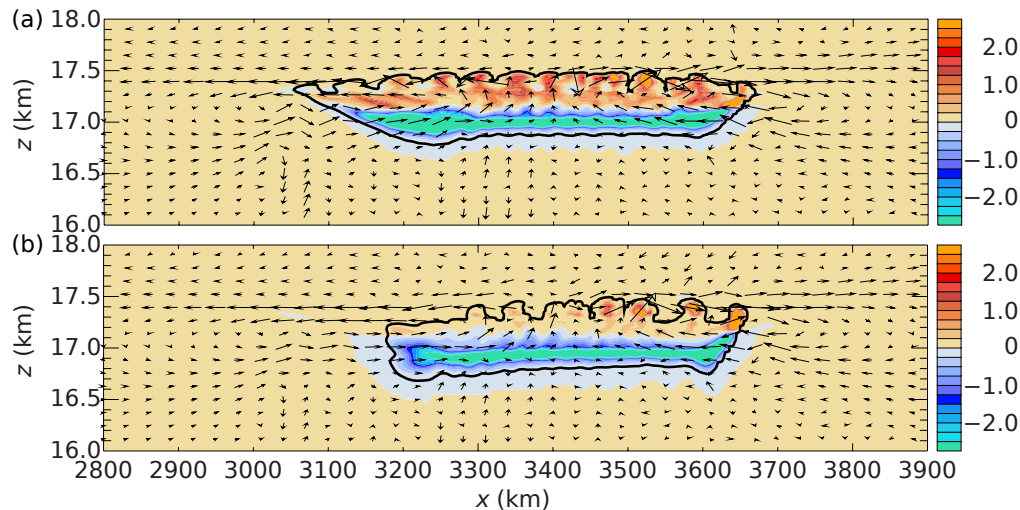


Fig. 14. Instantaneous latent heat release (10^{-8} K s^{-1}) at 3.5 day in the all-physics case **(a)** and in the no-RAV case **(b)**. The thick, black contour marks the cloud boundary, which is defined by the 1 l^{-1} contour of ice number concentration. Vectors show the radiatively induced velocities.

[Title Page](#)[Abstract](#)[Introduction](#)[Conclusions](#)[References](#)[Tables](#)[Figures](#)[◀](#)[▶](#)[◀](#)[▶](#)[Back](#)[Close](#)[Full Screen / Esc](#)[Printer-friendly Version](#)[Interactive Discussion](#)